

Optical Evaluation of the Rear Contacts of Crystalline Silicon Solar Cells by Coupled Electromagnetic and Statistical Ray-Optics Modeling

Ali Dabirian, Monica Morales-Masis, Franz-Josef Haug, Stefaan De Wolf, and Christophe Ballif

Abstract—High-efficiency crystalline silicon (c-Si) solar cells increasingly feature sophisticated electron and hole contacts aimed at minimizing electronic losses. At the rear of photovoltaic devices, such contacts—usually consisting of stacks of functional layers—offer opportunities to enhance the infrared response of the solar cells. Here, we propose an accurate and simple modeling procedure to evaluate the infrared performance of rear contacts in c-Si solar cells. Our method combines full-wave electromagnetic modeling of the rear contact with a statistical ray optics model to obtain the fraction of optical energy dissipated from the rear contact relative to that absorbed by the Si wafer. Using this technique, we study the impact of the refractive index, extinction coefficient, and thickness of the rear-passivating layer and establish basic design rules. In addition, we evaluate novel optical structures, including stratified thin films, nanoparticle composites, and conductive nanowires embedded in a low-index dielectric matrix, for integration into advanced rear contacts in c-Si photovoltaic devices. From an optical perspective, nanowire structures preserving low contact resistance appear to be the most effective approach to mitigating dissipation losses from the rear contact.

Index Terms—Crystalline Si photovoltaics, electromagnetic modeling, nanostructures, passivated emitter and rear cell (PERC), physical optics, silicon heterojunction (SHJ) solar cell.

I. INTRODUCTION

CRYSTALLINE silicon (c-Si) solar cells engineered for high conversion efficiencies increasingly feature advanced electron- and hole-collecting contacts [1]–[19]. The principal aim of such contacts is selective collection of one type of carrier, while avoiding recombination of the opposite carrier type [1], [2]. Ideally, carrier collection should occur without resistive losses. Silicon heterojunction (SHJ) solar cells exploit such passivating contacts. They use silicon wafers as optical absorbers and thin-film deposition to form contacts [1], [5]–[7]. In the most straightforward SHJ design, the electron and hole contacts are fabricated on the opposite sides of the wafer. Using this simple architecture, researchers from Kaneka Corporation (Japan) recently reported a power conversion efficiency of 25.1% from large-area wafers [13]. This high efficiency is largely linked to the passivating nature of the contacts, consisting of stacks of intrinsic/doped hydrogenated amorphous silicon, which is required for surface passivation and carrier collection. Both front and rear contacts are usually capped with transparent conductive oxides (TCOs) to maximize light coupling into the wafer and to minimize resistive losses from the collected carriers on their way either to the metal grids at the front, or to the metal electrode at the rear [1], [2], [14].

The rear metal electrode of an SHJ is often blanket deposited on TCO. In so-called “passivated emitter and rear cell” (PERC) c-Si solar cells, a patterned dielectric stack (e.g., consisting of a selection of SiO_2 , AlO_x , and SiN_x layers), rather than TCO, is often used at the rear [20]–[33]. In both structures, on textured layers, the dominant optical losses from the rear contact are associated with coupling of the incident light to the metal electrode through evanescent coupling [14]–[19]. This is an electromagnetic effect; full-wave modeling of this part of the device by solving Maxwell’s equations is thus necessary [18]. However, because the thickness of the Si wafer in c-Si solar cells is usually greater than 100 μm , modeling the entire device by performing full-wave calculations is computationally intensive. Several commercial and research solutions that combine electromagnetic modeling with ray-tracing techniques have recently been proposed to decrease the computational burden [34]–[38]. Although these methods are accurate, they require knowledge

Manuscript received October 25, 2016; revised January 9, 2017; accepted January 23, 2017. Date of publication February 15, 2017; date of current version April 19, 2017. This work was supported in part by the European Commission (FP7 project HERCULES under Grant 608498 and CHEETAH project under Grant 609788), in part by CCEM through Connect PV project, in part by the Swiss Federal Office for Energy, in part by the U.S. Department of Energy under the FPACEII project, and in part by the King Abdullah University of Science and Technology.

A. Dabirian is with the Photovoltaics and Thin-Film Electronics Laboratory, Institute of Microengineering, Ecole Polytechnique Fédérale de Lausanne, Neuchâtel 2002, Switzerland, and also with the School of Physics, Institute for Research in Fundamental Sciences, Tehran 19395-5531, Iran (e-mail: dabirian@ipm.ir).

M. Morales-Masis, F.-J. Haug, and C. Ballif are with the Photovoltaics and Thin-Film Electronics Laboratory, Institute of Microengineering, Ecole Polytechnique Fédérale de Lausanne, Neuchâtel 2002, Switzerland (e-mail: monica.moralesmasis@epfl.ch; franz-josef.haug@epfl.ch; christophe.ballif@epfl.ch).

S. De Wolf is with the KAUST Solar Center, King Abdullah University of Science and Technology, Thuwal 23955-6900, Saudi Arabia (e-mail: stefaan.dewolf@kaust.edu.sa).

Color versions of one or more of the figures in this paper are available online at <http://ieeexplore.ieee.org>.

Digital Object Identifier 10.1109/JPHOTOV.2017.2663658

of both ray tracing and electromagnetic modeling, along with the complicated routines needed to couple these two models.

Here, we introduce a simple, alternative procedure to estimate dissipation losses from the rear contact of c-Si solar cells. Our procedure basically treats the interaction of light with the rear-contact stack as an electromagnetic phenomenon. The obtained electromagnetic solutions are then plugged into a statistical ray-optics formulation [39] to take into account the effect of light propagation in the textured Si wafer. This simple modeling routine has a significant advantage during the design of photovoltaic devices because it allows optimization of different rear-contact designs. We confirm the accuracy of our modeling technique by comparing modeling results with experimental measurements. In Section II, we describe the modeling procedure along with device configuration. We then use this modeling procedure in Section III to study how the refractive index, extinction coefficient, and the thickness of the rear contact layers affect the parasitic absorption losses from the rear contact. In Section IV, we use the refractive indices of actual materials, such as $\text{In}_2\text{O}_3:\text{Sn}$ (ITO) and SiO_2 , to evaluate a number of practical structures for potential use as rear contacts of c-Si solar cells. In Section V, conclusions are presented.

II. MODELING APPROACH

A schematic of a standard textured c-Si solar cell is shown in Fig. 1. The device is composed of a textured Si wafer with doped layers/regions on both sides of the wafer. PERC-type c-Si cells are created either by diffused or ion-implanted impurity doping [40], followed by dielectric passivation-layer deposition, and capping of the rear dielectric by full-area metallization. Both front and electrical rear contacts are locally adhered to the silicon wafer underneath. At the rear, since the coverage of the localized contacts is typically around 1% of the surface area, we may neglect local features in our optical considerations. In SHJ cells, the wafer is covered with thin stacks of doped and intrinsic a-Si thin films, TCOs, and the metallized layer [1]. This specific architecture does not require local contact formation, as the full layer stack acts as a passivating contact. In the standard configuration, the front TCO is usually a high-mobility compound and it is covered by a metallic grid to transport the electrical current to the load. In case the full area of the rear contact is metallized, the rear TCO needs only to provide transverse (and not lateral) conduction, and it should be highly transparent such that infrared light can mitigate parasitic absorption losses [15]–[19].

The rear contact is essentially a stratified medium comprising three materials: Si, a dielectric, and a metal [see Fig. 1(c)]. We model this part with full-wave electromagnetic modeling. We restrict our consideration of the type of rear reflector metal to Ag and obtain the complex refractive index from the literature [41]. The incident light is modeled as a plane wave, mathematically described by $\vec{E} = \hat{y}E_{0y}\exp[-jk_0z\cos(\theta)]$, where θ is the angle of incidence and $k_0 = 2\pi/\lambda$ is the wavenumber. This is a transverse-magnetic (TM) electromagnetic wave because its magnetic vector is perpendicular to the plane of wave propagation [see Fig. 1(c)]. Transverse electric (TE) polarization is essentially the same with \vec{E} and \vec{H} interchanged in the schematic

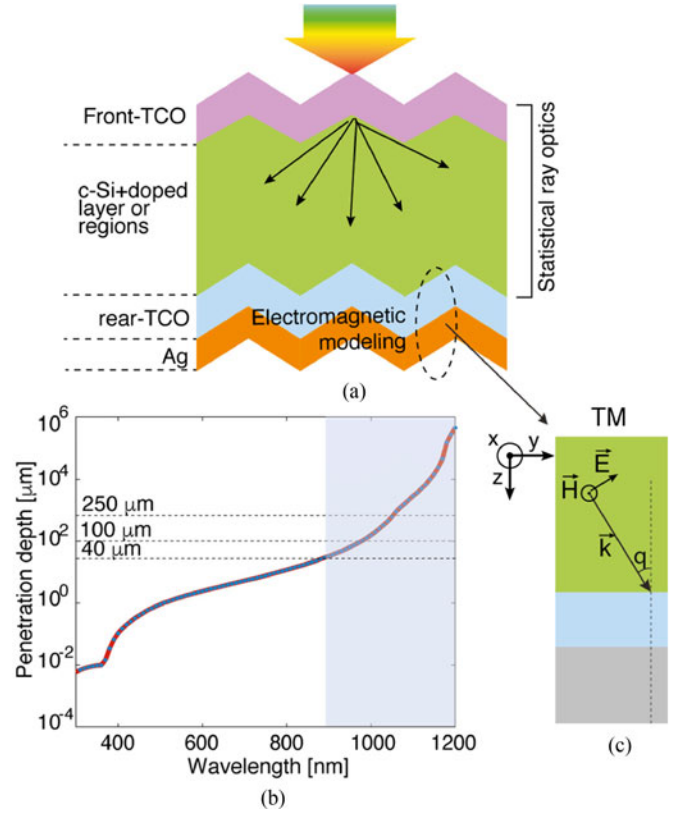


Fig. 1. (a) A schematic of a textured crystalline (heterojunction) Si solar cell in which different simulation-relevant layers are specified. (b) The penetration depth of light in crystalline Si. (c) A schematic of light incidence from TM-polarized waves on the rear side of a solar cell.

in Fig. 1(c). The losses from the rear contact associated with TE-polarized light incidence are a few orders of magnitude smaller than those of TM-polarized light incidence [17], [18].

The electromagnetic fields of TM and TE waves in a multi-layer stratified medium have an analytical solution [42], [43]. In our modeling, the optical absorption in the TCO and Ag layer is the most important parameter, designated as $\eta_{\text{TCO}}(\lambda, \theta)$ and $\eta_{\text{Ag}}(\lambda, \theta)$, respectively. They are defined and calculated by integration of the power absorption density, $p_d(\text{Ag, TCO}) = (\frac{1}{2})\omega\epsilon''_{\text{Ag, TCO}}|\vec{E}|^2$, over the entire volume of the respective layer; i.e., TCO or Ag, where \vec{E} is the electric field, ϵ'' is the imaginary part of a given material's permittivity, and $\omega = 2\pi/\lambda$ is the angular frequency of light.

The light enters the device from the front side and in the infrared wavelength range [$\lambda > 900$ nm for a 250-μm-thick wafer, see Fig. 1(b)] it partially passes through the wafer and interacts with the rear TCO and Ag layers. Upon reflectance from this part, the light acquires a different angle of propagation from its original one. In a textured Si solar cell, the rear contact is not a planar stratified medium but a stratified medium with a morphology of random pyramids. This morphology is developed during the chemical cleaning of the Si wafer and removal of saw damage and it can be adjusted to a certain extent by varying the chemical compounds used. A widely accepted approximation is that the reflected light from the rear contact

of a textured Si solar cell can be described by a Lambertian distribution [17], [18]. Accurate evaluations have shown that the contribution of specular reflection to the first two internal reflections is rather strong and the distribution comes close to Lambertian only after these reflections [44]. The effect of the delayed Lambertian distribution on the overall performance of the device is not significant, however. Therefore, to acquire an estimate of rear-contact losses that is close to reality, the optical absorption calculated using electromagnetic modeling is averaged by the angular distribution as follows [39]:

$$\langle \eta_i \rangle_\theta (\lambda) = \int_0^{\pi/2} \eta_i (\lambda, \theta) \sin(\theta) \cos(\theta) d\theta \quad (1)$$

where η_i can be η_{Ag} , η_{TCO} , or $\eta_{\text{Ag}} + \eta_{\text{TCO}}$. $\sin(\theta)$ in the formula comes from the definition of the solid angle, i.e., $d\Omega = \sin(\theta) \cos(\varphi) d\theta d\varphi$ in which φ varies from 0 to 2π radians leading to $d\Omega = \sin(\theta) d\theta \cos(\theta)$ expresses the projection of the emitting surface in the direction of the observer [39].

Our goal is to evaluate the impact of absorption losses in the rear contact relative to the desired absorption in the bulk of the Si wafer. For simplicity, the primary reflectance from the (front) wafer surface is neglected. If we apply these assumptions and simplifications to the statistical ray-optics relations derived by Yablonovitch [39], the fraction of the incoming light absorbed by the Si wafer [$f_{\text{Si}}(\lambda)$] can be separated from the part absorbed by the rear contact [$f_{\text{Loss}}(\lambda)$]. These parameters are described by [32]

$$f_{\text{Si}}(\lambda) = \frac{2\alpha_{\text{Si}}(\lambda) t_{\text{Si}}}{\left[\frac{1}{2n_{\text{Si}}^2(\lambda)} + \langle \eta \rangle_\theta (\lambda) + 2\alpha_{\text{Si}}(\lambda) t_{\text{Si}} \right]} \quad (2)$$

and

$$f_{\text{Loss}}(\lambda) = \frac{\langle \eta \rangle_\theta (\lambda)}{\left[\frac{1}{2n_{\text{Si}}^2(\lambda)} + \langle \eta \rangle_\theta (\lambda) + 2\alpha_{\text{Si}}(\lambda) t_{\text{Si}} \right]} \quad (3)$$

where $\eta = \eta_{\text{Ag}} + \eta_{\text{TCO}}$, $\alpha_{\text{Si}}(\lambda)$ is the optical absorption coefficient of c-Si, t_{Si} is the thickness of the Si wafer, and $n_{\text{Si}}(\lambda)$ is the refractive index of c-Si at wavelength λ . In fact, $f_{\text{Si}}/f_{\text{Loss}}$ can be used as a figure of merit (FOM) for evaluating the optical quality of the rear contact of c-Si solar cells. This FOM can be simplified to $\text{FOM}(\lambda) = 2\alpha_{\text{Si}}(\lambda) t_{\text{Si}} / \langle \eta \rangle_\theta (\lambda)$.

A fraction of the light that is internally reflected from the rear contact can still escape from the front side of the cell (f_{ESC}). This part also appears in Yablonovitch's statistical ray-optics model. In the c-Si solar cell studied here, this light fraction can be calculated from $f_{\text{ESC}} = 1 - f_{\text{Loss}} - f_{\text{Si}}$. It should be noted that f_{ESC} does not include the external reflectance from the front side of the cell.

For device design, a more relevant evaluation is obtained by comparing optical losses in terms of the equivalent current density. To obtain such associated current densities, the fractional absorptions are weighed by the spectrum of air mass 1.5 global (AM1.5G) irradiation and integrated over the wavelength range of interest as follows [38]:

$$\langle f_i \rangle_{\text{AM1.5G}} = \frac{e}{hc} \int_{\lambda_{\text{st}}}^{\lambda_{\text{sp}}} f_i(\lambda) \phi_{\text{AM1.5G}}(\lambda) \lambda d\lambda \quad (4)$$

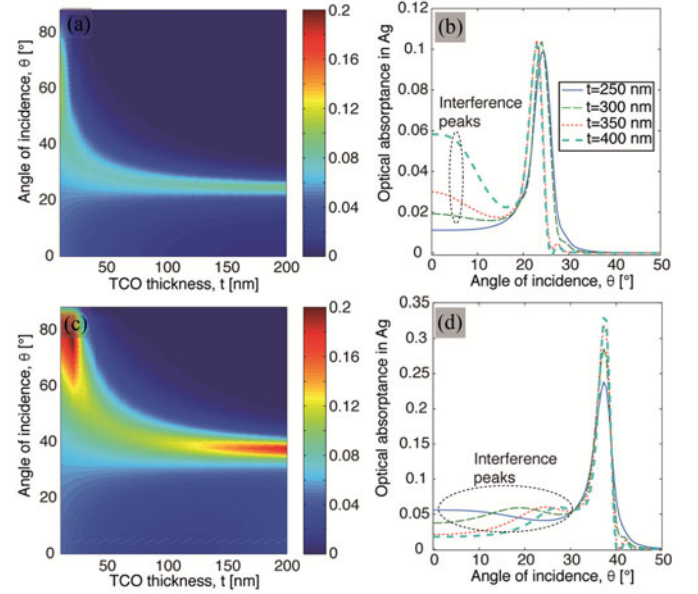


Fig. 2. Optical absorptance of Ag at $\lambda = 1100$ nm if the TCO thickness varies from 10 to 400 nm for two different TCO refractive indices: (a) and (b) $n = 1.37$; (c) and (d) $n = 2$.

where f_i can be f_{Si} , f_{Ag} , or f_{Loss} , e is the elemental charge, h is Planck's constant, c is the speed of light, $\phi_{\text{AM1.5G}}(\lambda)$ is the AM1.5G irradiation spectrum, and λ_{st} , λ_{sp} are the limits of the wavelength range of study. This parameter is equivalent to the upper limit of short-circuit current density generated by the spectral portion of AM1.5G light in the λ_{st} to λ_{sp} wavelength range, under a 1 sun intensity assuming the ideal case of 100% charge collection efficiency.

III. PHYSICAL EFFECTS

In this section, we use the model described in Section II to study how the refractive index, extinction coefficient, and thickness of the rear-TCO layer of a c-Si solar cell affect the parasitic optical absorption of the rear contact. Based on these results, we then establish basic design rules to minimize rear-contact optical losses.

A. Effect of TCO Layer Thickness

In this part, we assume that the TCO layer is a lossless dielectric ($k = 0$); thus, the rear-contact losses are caused only by the Ag layer. These losses can be significant with high angles of incidence, but their impact can be reduced to evanescent coupling by the insertion of a dielectric layer [15]. We, thus, expect that at a fixed refractive index, the rear-contact losses can be reduced by increasing the thickness of the dielectric layer.

Fig. 2 shows the optical absorption in the Ag layer (η_{Ag}) as the angle of incidence and the thickness of the dielectric layer vary with two refractive indices of 1.37 and 2 (values at $\lambda = 1100$ nm). These values correspond to the refractive indices of MgF_2 and idealized, typical undoped TCOs (e.g., ITO or ZnO), respectively. The losses appear as broad peaks at low TCO thicknesses. However, as the thickness of the layer

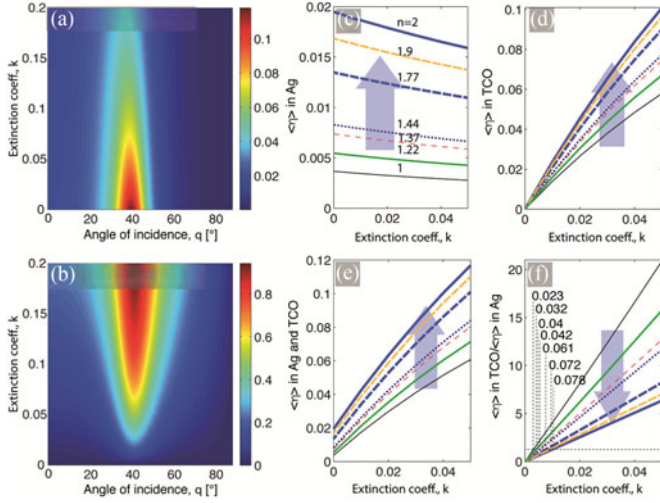


Fig. 3. Optical absorbance at $\lambda = 1100$ nm in (a) Ag and (b) TCO with a TCO refractive index of 2 and thickness of 100 nm as the extinction coefficient varies from 0 to 0.2. The variation of integrated optical absorption $\langle \eta \rangle_\theta(\lambda)$ in (c) Ag, (d) TCO, (e) the summation and (f) the ratio of the two as the extinction coefficient varies in the 0–0.1 range at different refractive indices from 1 to 2. The smaller range of k is shown in (c)–(f) to better illustrate the optical absorption values at lower k values. The direction of the blue arrow indicates the trend of variations with increasing TCO refractive index.

increases beyond $\lambda/4n_{\text{TCO}}$, effects of interference can occur in the dielectric layer. The interference leads to multiple interactions of light with the Ag layer, hence leading to an undesired increase in optical absorption, particularly at lower angles of incidence [see Fig. 2(b) and (d)]. We, therefore, set the upper limit on the thickness of the dielectric layer from the onset of optical interference in the layer.

B. Effect of TCO Loss

Previous studies on lossless rear-TCO materials showed that the smaller the refractive index of such materials, the lower the rear-contact losses [16]. However, practical TCOs often exhibit considerable optical absorption associated with their bulk, particularly in the infrared wavelength range due to the presence of free charge carriers.

Fig. 3(a) and (b) shows the color plots of optical absorbance at $\lambda = 1100$ nm in TCO and Ag layers of a hypothetical TCO/Ag stack with a TCO refractive index of 2 and a thickness of 100 nm as the angles of incidence and TCO extinction coefficient vary from 0° to 90° and from 0 to 0.2, respectively. In both cases, the absorbance shows a peak near the angle of total internal reflectance (TIR), defined as $\theta_{\text{TIR}}(\lambda) = \arcsin[n_{\text{TCO}}(\lambda)/n_{\text{Si}}(\lambda)]$. η_{Ag} decreases as the extinction coefficient k of the TCO increases, whereas η_{TCO} increases. The angular average of the optical absorption of Ag, TCO, and the summation of the two show that 1) the overall optical absorption in the rear contact increases as k increases and that 2) the TCO with the lower refractive index exhibits lower optical absorption at similar k values. Fig. 3(f) shows the ratio of $\langle \eta_{\text{TCO}} \rangle_\theta$ to $\langle \eta_{\text{Ag}} \rangle_\theta$, revealing that at $k > 0.01$, the optical absorption of the TCO bulk becomes the dominant part of the optical absorption of the total stack. We used the refractive index of bulk Ag in our

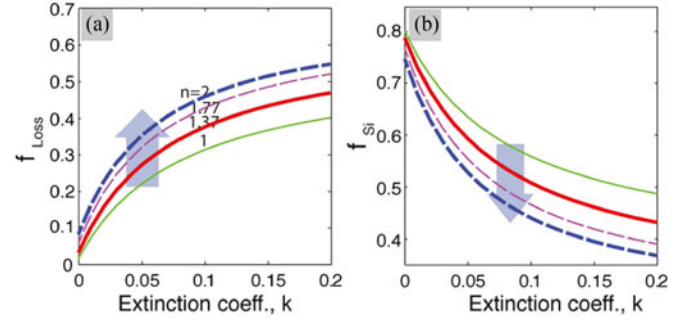


Fig. 4. (a) Fractional losses from the rear contact and (b) fractional optical absorption of a 250- μm -thick Si wafer as the extinction coefficient of the 100-nm-thick TCO of different refractive indices (n) varies from 0 to 0.2 calculated at $\lambda = 1100$ nm.

calculations; however, we note that the refractive index of sputtered Ag thin films deviates slightly from that of the bulk. In an actual device, the exact values of the losses from both TCO and Ag layers may, therefore, be slightly different from our calculated data.

The impact of a nonzero k -value of the TCO is clearly shown when we consider the TCO/Ag stack as the rear contact of a 250- μm -thick c-Si wafer: The fraction of optical absorption by TCO (see Fig. 4) quickly increases with increasing the k -value of TCO, which leads to a dramatic drop in the fraction of light absorbed by the Si. We, therefore, suggest that to minimize parasitic absorption losses, the absorption losses in the bulk TCO should be minimized. Only then does lowering the refractive index to further minimize the losses from the rear-contact of the c-Si solar cell makes sense. This particularly applies to SHJ cells in which a conductive TCO layer is needed on the rear side. On the contrary, in PERC cells, the Al_2O_3 layer is almost lossless in the infrared range up to $\lambda = 1200$ nm. Furthermore, the summation of f_{Si} and f_{LOSS} is not unity because the calculation takes into account the fraction of light that can escape from the solar cell's front side (f_{ESC}) after being internally reflected from the cell's rear side.

IV. EVALUATION OF DIFFERENT REAR CONTACTS

In this section, we evaluate practical TCO materials with dispersive n - and k -values. These materials include ITO with different carrier densities. ITO is the most widely used TCO in SHJ c-Si solar cells. We compare the calculated data for ITO with experimentally measured quantum efficiencies to validate our calculations [1], [16]. In addition, we studied stacks of ITO with different carrier densities as well as anisotropic composites of SiO_2 and ITO—either as nanoparticles or as nanowires—to obtain TCOs with lower refractive indices and higher transparency. We restrict our study to rear TCOs with 100-nm thicknesses, which is sufficiently thick to largely suppress plasmonic losses. Sufficient insight can be obtained about the impact of TCO thickness by considering these results together with the results in Fig. 2.

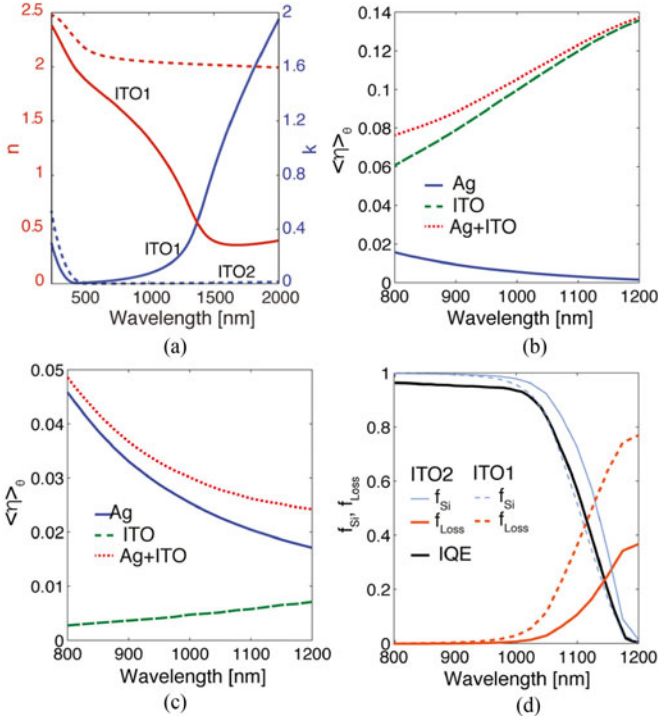


Fig. 5. (a) The real and imaginary parts (n and k) of the refractive index spectra of ITOs with two different carrier concentrations [7]. The spectra of integrated optical absorption $\langle \eta \rangle_\theta(\lambda)$ in Ag, TCO, and the rear-contact (ITO + Ag) for (b) ITO1 and (c) ITO2 as the rear TCO. The spectra of fractional optical absorption in the rear-contact and the Si wafer for the two different rear TCOs of ITO. The internal quantum efficiency spectrum of a typical SHJ cell with a front ITO and rear TCO added for reference.

A. ITO Layers

Indium tin oxide with 10 wt% Sn doping is regularly used as the rear TCO in SHJ solar cells [1]. Here, we focus on two ITO films with different carrier densities [$2.4 \times 10^{20} \text{ cm}^{-3}$ (ITO1) and $1.7 \times 10^{19} \text{ cm}^{-3}$ (ITO2)], of which the associated refractive indices are taken from the literature [16]. The spectra of the n - and k -values of the two ITO films are shown in Fig. 5(a).

These ITO layers (100-nm thick) are applied as part of the rear contacts of c-Si solar cells on 250- μm -thick Si wafers. The $\langle \eta \rangle_\theta$ spectra show that absorption by ITO1 is the dominant loss, whereas absorption by Ag is the dominant loss in ITO2 [see Fig. 5(b) and (c)]. Moreover, the total rear-contact optical absorption losses in the cell with ITO1 are significantly higher than those in the cell with ITO2, despite the fact that ITO1 has a lower refractive index in the infrared range. This result underscores that optical absorption losses from the TCO bulk constitute an important parameter that requires attention during the design of rear contacts of Si solar cells.

The fractional optical absorption of Si (f_{Si}) and the rear contact (f_{Loss}) indicate that f_{Si} is significantly higher in the device with the more transparent ITO2 as the rear-TCO compared with the device with the less transparent ITO1. f_{Si} is directly related to the internal quantum efficiency (IQE) of an actual device because the reflectance from the Si surface is neglected in our calculations. Essentially IQE is defined as the ratio of the number of charge carriers collected in a solar cell to the number of

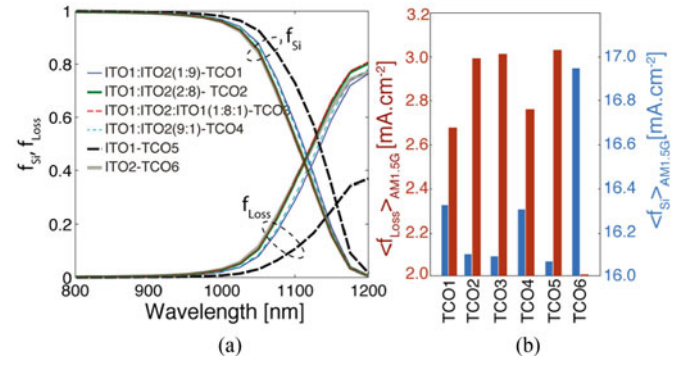


Fig. 6. (a) The spectra of f_{Si} and f_{Loss} when 100 nm of different ITO stacks are used as the rear TCO of a 250- μm -thick Si solar cell. (b) The equivalent current densities lost from the rear contact and absorbed by the Si wafer. The labels are defined in (a). The thicknesses of the rear TCO layer and Si wafer are 100 nm and 250 μm , respectively, in all cases.

photons absorbed in the Si wafer. In fact, f_{Si} shares a similar definition when we assume that the collection of charge carriers is 100% efficient. The IQE spectra of an SHJ solar cell [16] are in close agreement with the calculated f_{Si} . The small discrepancy is associated with the optical absorption by the front TCO that has not been taken into account in our model.

B. Stratified TCO layers

When new TCOs aimed at combining low optical absorption and low refractive index are designed, their electrical properties—in particular their work function—can change significantly. Such changes could detrimentally affect the formation of the electrical contacts and thus the charge transport from Si to TCO, which would appear in a performance graph as s-shaped current–voltage characteristics [19], [45]. Often, such an issue can be resolved by inserting a thin “standard” TCO between the new TCO and the Si. The interaction of light with such a multilayered TCO can be studied in the general context of stratified TCO layers.

To study how stacks of different TCOs optically function as rear TCOs, we studied a number of stacks with a fixed total thickness (100 nm), including ITO1(10 nm)/ITO2(90 nm)/Ag, ITO2(90 nm)/ITO1(10 nm)/Ag, ITO1(10 nm)/ITO2(80 nm)/ITO1(10 nm)/Ag, and finally ITO1(20 nm)/ITO2(80 nm)/Ag. In these stacks, the ITO1 (with a high carrier density) was used on one side or on both sides of ITO2 (with a low carrier density) to facilitate charge transport across the interfaces [15], [45].

The spectra of f_{Si} , f_{Loss} , and their equivalent short-circuit current densities (i.e., $\langle f_{\text{Loss}} \rangle_{\text{AM1.5G}}$ and $\langle f_{\text{Si}} \rangle_{\text{AM1.5G}}$) are shown in Fig. 6. These spectra indicate that the presence of ITO1 in all cases dramatically increased rear-contact losses relative to a 100-nm ITO2 layer. Notably, the most influential parameter is the amount of ITO1 and not its precise location in the stack. In all the studied cases, we partially attribute the optical loss induced by the thin ITO1 layer to the functioning of this layer as a low-refractive nanostructure that traps light due to its small dimensions [46]. In such a structure, an ultrathin low-refractive index layer (ITO1) sandwiched between two higher refractive index materials (Si and ITO2) traps the light. This effect leads

to large optical absorption by the stratified TCO layers despite the relatively small fraction of absorbing ITO1 layers present in the stack. Of course, the absolute amount of the absorption scales with the amount of ITO1.

C. Nanoparticle Composites

Nanoparticle composites combine the optical and electrical properties of different materials to obtain optimal material properties. A practical solution to reducing the refractive index of TCOs is to mix them with a low-refractive index material such as SiO₂ (with a refractive index around 1.44 in the visible spectrum). The mixture of SiO₂ with TCO was studied by mixing the materials using sputtering [19] to yield a homogeneous mixture. However, an SiO₂ concentration greater than 8.6 mol% was shown to deteriorate the electrical conduction dramatically [19]. The formation of a nanoparticle composite comprising a percolating network of TCO particles in an SiO₂ matrix could lead to conductive layers with higher SiO₂ content. To achieve conduction, the content of the conducting nanoparticles should exceed the percolation threshold, which is estimated to be more than 15 vol% [47], [48]. We, therefore, compare composites of SiO₂ and ITO1 with ITO1 volumetric ratios of 15%, 20%, 25%, and 30%.

To analyze structures using the method we propose here, the composite layer needs to be described by the *effective medium* refractive index and extinction coefficient values. We used the Maxwell–Garnett theory to obtain the effective medium refractive index values. The effective index, described as the square root of the effective permittivity, is obtained by [49]

$$\left(\frac{\epsilon_{\text{eff}} - \epsilon_{\text{SiO}_2}}{\epsilon_{\text{eff}} + 2\epsilon_{\text{SiO}_2}} \right) = p_{\text{ITO}} \left(\frac{\epsilon_{\text{ITO}} - \epsilon_{\text{SiO}_2}}{\epsilon_{\text{ITO}} + 2\epsilon_{\text{SiO}_2}} \right) \quad (5)$$

where p_{ITO} is the volume fraction of ITO nanoparticles.

The f_{Si} and f_{Loss} spectra show that variation of the ITO1 volume fraction from 30% to 15% reduces the rear-contact losses along with a slightly lower improvement in the light absorbed by Si [see Fig. 7(b)]. This variation leads to 0.5 mA/cm² gain in the amount of AM1.5G light absorbed by the 250- μm -thick Si wafer in comparison with when the rear-TCO is ITO1 only. This improvement is quite significant. However, this strategy does not lead to sufficiently low refractive indices, mainly because a relatively high concentration of ITO1 nanoparticles is needed in the composite to surpass the percolation threshold. We, therefore, expect that nanoparticle composites will not yield much more improvement relative to the composites synthesized by established processes in the c-Si solar cell industry, such as sputtering [19].

An alternative approach is to grow porous oxides that are viewed optically as a mixture of oxide nanoparticles and air [49]–[51]. These structures can in principle lead to TCO layers with refractive index values very close to that of air, i.e., 1. The question is whether lowering the refractive index to this value can lead to a meaningful increase in the cell's photocurrent density.

Fig. 8 compares f_{Si} , f_{Loss} , and f_{ESC} for ITO2, SiO₂, and air as a rear contact of a 250- μm -thick Si wafer. By comparing SiO₂

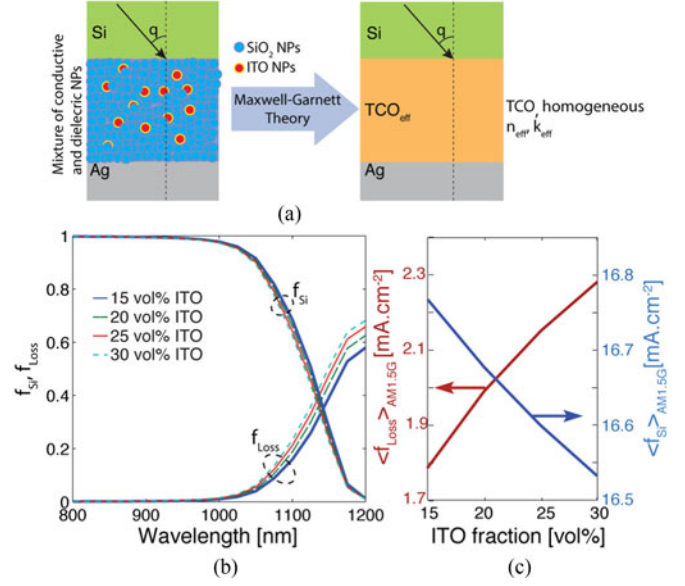


Fig. 7. (a) Schematic of a rear contact composed of a mixture of ITO1 and SiO₂ nanoparticles as the rear TCO. (b) Spectra of f_{Si} and f_{Loss} and (c) the equivalent current densities of Si and the rear-contact loss for SiO₂ and different volume fractions of ITO1 nanoparticles in SiO₂. The thicknesses of the SiO₂/ITO layer and the Si wafer are 100 nm and 250 μm , respectively, in all cases.

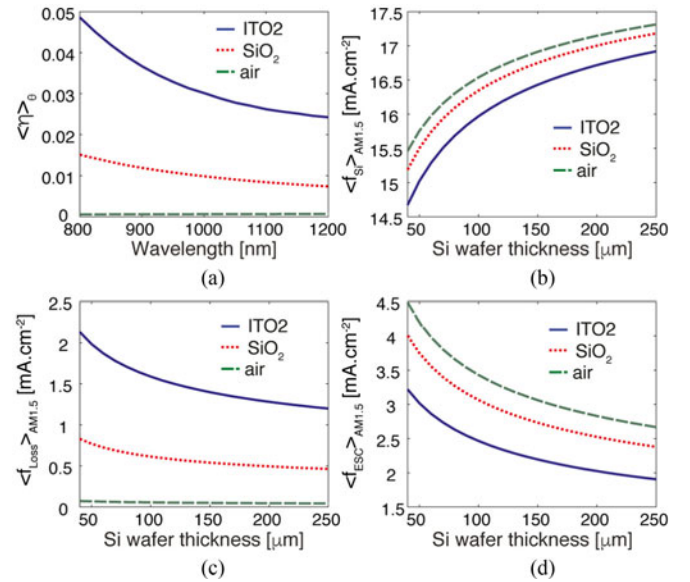


Fig. 8. (a) The $\langle \eta \rangle_{\theta}(\lambda)$ spectra of the rear contact of 100 nm of ITO1, SiO₂, and air ($n = 1$). The equivalent current densities of the light absorbed by (b) the Si wafer and (c) the rear contact as well as the current density of the light that escapes from the cell upon reflection from the rear contact.

with air, we see that f_{Loss} does significantly decrease. However, this decrease does not translate into an equivalent amount of increase in f_{Si} ; it largely contributes to f_{ESC} . This means that the recovered f_{Loss} of TCOs with refractive indices lower than that of SiO₂ mostly contributes to f_{ESC} . This suggests another practical limit related to the infrared quantum efficiency of Si solar

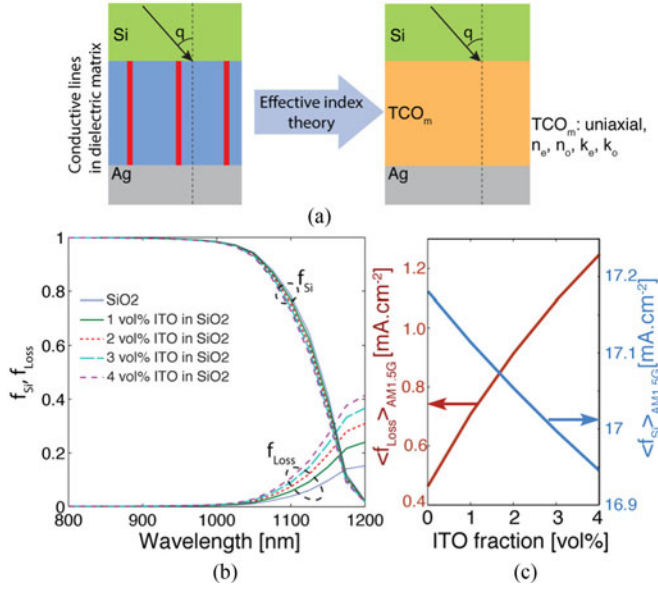


Fig. 9. (a) Schematic of a rear contact with ITO1 nanowires embedded in a SiO₂ matrix as the rear TCO. (b) f_{Si} and f_{Loss} spectra and (c) the equivalent current densities of Si and the rear-contact loss for SiO₂ and different volume fractions of ITO1 nanowires in SiO₂. The SiO₂/ITO layer and Si wafer thicknesses are 100 nm and 250 μ m, respectively, in all cases.

cells: once the rear-contact losses are almost completely annihilated, the front contact becomes the dominant location for losses. When air instead of TCO is used in the rear contact, the loss at the rear may be as low as $\eta < 0.001$ over the entire spectrum, but the improvement in $\langle f_{Si} \rangle_{AM1.5G}$ of a 250- μ m-thick Si wafer relative to that of SiO₂ rather than TCO is only 0.13 mA/cm². Developing and utilizing TCOs with extremely low refractive indices (i.e., lower than that of SiO₂) is not expected to lead to meaningful improvements in the optical absorption of the cell and, hence, in the cell's photocurrent density.

D. Nanowires Embedded in a Dielectric Matrix

Even though the percolation limit for the conducting nanocomposites is only 15% of that of ITO, Fig. 7 suggests that the rear-contact losses cannot be reduced below 1.8 mA/cm². The ITO content may be further reduced in the case of a nanowire compound in which conductivity does not rely on a randomly generated percolation path but on transversally aligned nanowires. We, therefore, evaluate ITO1-type nanowires embedded in an SiO₂ matrix [see Fig. 9(a)]. The effective index of the layer is again obtained by the Maxwell–Garnett theory, this time of a uniaxial medium [42] because in this anisotropic layer, the refractive indices along and across the nanowires are different. The refractive indices along and across the nanowires are referred to as in-plane ($n_{o,eff}$) and out-of-plane ($n_{e,eff}$) refractive indices, respectively, and they are obtained from the square root of their corresponding permittivity values described by the following formula [42]:

$$\epsilon_{o,eff} = p_{ITO} + (1 - p_{ITO}) \epsilon_{SiO_2} \quad (6)$$

and

$$\frac{1}{\epsilon_{e,eff}} = \frac{p_{ITO}}{\epsilon_{ITO}} + \frac{(1 - p_{ITO})}{\epsilon_{SiO_2}} \quad (7)$$

where p_{ITO} is the volume fraction of ITO nanowires in the SiO₂ matrix.

Fig. 9(b) shows the f_{Si} and f_{Loss} spectra for a 250- μ m-thick Si wafer with 100 nm of either SiO₂ or a composite of SiO₂ with different fractions of ITO1 on the rear side between the Si and Ag. These spectra show that the rear-contact optical losses are strongly reduced pure SiO₂ is used due to its low refractive index and high transparency. Addition of the ITO1 nanowires leads to an increase in the rear-contact losses, from 0.47 to 1.1 mA/cm² of J_{sc} loss when 4 vol% ITO nanowires is added. The impact on the amount of light absorbed by Si is less dramatic when the rear-TCO loss due to addition of up to 4 vol% ITO1 nanowires leads to a 0.27 mA/cm² decrease in amount of the light absorbed by the Si. The reason for this is that, in this case, the fraction of light escaping from the front side of the Si wafer limits the optical absorption by Si. The optical absorption by Si continues to increase as the rear-TCO refractive index decreases below that of SiO₂. This is an indication that rear reflector is close to ideal. However, from a practical point of view, this increase is not significant.

Maintaining sufficient electrical conductivity across the layer thickness is essential for proper functioning of the cell. However, electrical conductivity cannot be quantified using the calculations presented here. In fact, electrical conductivity puts a limit on the minimum fraction of the conductive nanowires that is necessary as has been observed in composited ZnO:Al–SiO₂ prepared by sputtering [19].

V. CONCLUSION

We proposed and validated a fully analytical model for calculating the rear-contact losses of c-Si solar cells. Our method combines electromagnetic optics treatment of thin-film layers with the statistical ray-optics formulation of light propagation in the thick c-Si wafer. The main findings relevant to designing new rear TCOs are as follows: 1) the thickness of the rear TCO should not exceed $\lambda/4n_{dielectric}(\lambda)$ to hinder losses induced by optical interference and 2) the transparency of the TCO (i.e., its k -value) has profound impact on losses from the rear contact. A rear TCO comprising alternating layers of highly transparent and highly conductive TCOs does not lead to significant improvement because the optical losses from the highly conductive TCO mainly determine rear-contact losses. Nanoparticle composites are not a useful alternative material due to the large number of conductive particles needed to achieve percolation. Conductive nanowires embedded in a dielectric matrix constitute a better alternative because the percolation limit is increased. Finally, decreasing the refractive index of rear TCOs below that of SiO₂ does not lead to significant improvement in short-circuit current density despite a decrease in rear-contact losses because light escaping from the front of the Si wafer limits the optical absorption of Si. Our findings are particularly important to optimizing

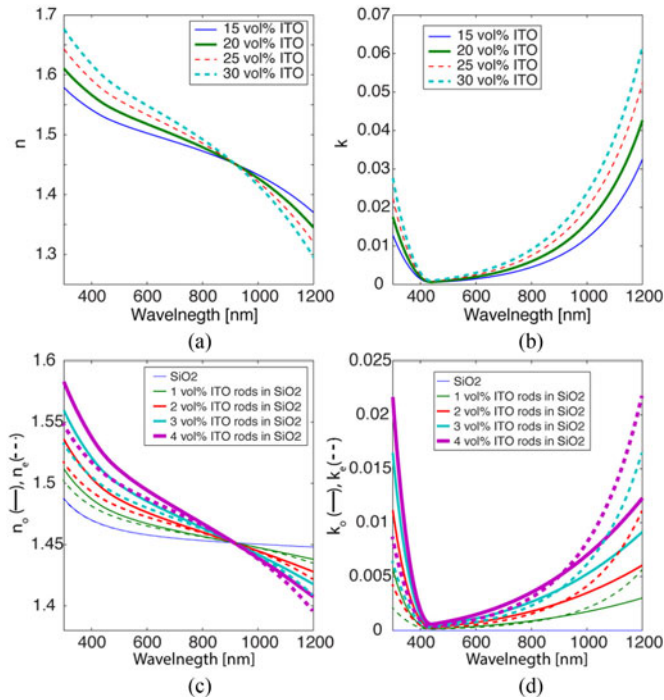


Fig. 10. Effective refractive index and extinction coefficient for (a), (b) nanoparticle composite and (c), (d) nanowire composite.

SHJ and PERC solar cells with rear contacts composed of a stack of TCO (or dielectric) and metal.

APPENDIX

The effective refractive index values calculated for the nanoparticle composites and the nanowire composites are presented in Fig. 10. The refractive index of SiO_2 [19] is shown in Fig. 10(c).

REFERENCES

- [1] S. De Wolf, A. Descoeurdes, Z. C. Holman, and C. Ballif, "High-efficiency silicon heterojunction solar cells: A review," *Green*, vol. 2, pp. 7–24, 2012.
- [2] C. Battaglia, A. Cuevas, and S. De Wolf, "High-efficiency crystalline silicon solar cells: Status and perspectives," *Energy Environ. Sci.*, vol. 9, pp. 1552–1576, 2016.
- [3] A. Dabirian *et al.*, "Metallization of Si heterojunction solar cells by nanosecond laser ablation and Ni-Cu plating," *Sol. Energy Mater. Sol. Cells*, vol. 159, pp. 243–250, 2017.
- [4] K. Masuko *et al.*, "Achievement of more than 25% conversion efficiency with crystalline silicon heterojunction solar cell," *IEEE J. Photovolt.*, vol. 4, no. 6, pp. 1433–1435, Nov. 2014.
- [5] A. Descoeurdes *et al.*, ">21% Efficient silicon heterojunction solar cells on n-type and p-type wafers compared," *IEEE J. Photovolt.*, vol. 3, no. 1, pp. 83–89, Jan. 2013.
- [6] C. Battaglia *et al.*, "Silicon heterojunction solar cell with passivated hole selective MoOx contact," *Appl. Phys. Lett.*, vol. 104, 2014, Art. ID. 113902.
- [7] J. Geissbuehler *et al.*, "22.5% efficient silicon heterojunction solar cell with molybdenum oxide hole collector," *Appl. Phys. Lett.*, vol. 107, 2015, Art. ID. 081601.
- [8] U. Romer *et al.*, "Recombination behavior and contact resistance of n^+ and p^+ poly-crystalline Si/mono-crystalline Si junctions," *Sol. Energy Mater. Sol. Cells*, vol. 131, pp. 85–91, 2014.
- [9] B. Nemeth *et al.*, "Polycrystalline silicon passivated tunneling contacts for high efficiency silicon solar cells," *J. Mater. Res.*, vol. 31, pp. 671–681, 2016.
- [10] J. Bullock *et al.*, "Efficient silicon solar cells with dopant-free asymmetric heterocontacts," *Nature Energy*, vol. 1, 2016, Art. ID. 15031.
- [11] X. Yang *et al.*, "High-performance TiO_2 -based electron-selective contacts for crystalline silicon solar cells," *Adv. Mater.*, vol. 28, pp. 5871–5877, 2016.
- [12] F. Feldmann *et al.*, "Tunnel oxide passivated contacts as alternative to partial rear contacts," *Sol. Energy Mater. Sol. Cells*, vol. 131, pp. 46–50, 2014.
- [13] D. Adachi, J. L. Hernández, and K. Yamamoto, "Impact of carrier recombination on fill factor for large area heterojunction crystalline silicon solar cell with 25.1% efficiency," *Appl. Phys. Lett.*, vol. 107, 2015, Art. ID. 233506.
- [14] S. De Wolf and M. Kondo, "Nature of doped a-Si:H/c-Si interface recombination," *J. Appl. Phys.*, vol. 105, 2009, Art. ID. 103707.
- [15] Z. C. Holman, A. Descoeurdes, S. De Wolf, and C. Ballif, "Record infrared internal quantum efficiency in silicon heterojunction solar cells with dielectric/metal rear reflectors," *IEEE J. Photovolt.*, vol. 3, no. 4, pp. 1243–1249, Oct. 2013.
- [16] Z. C. Holman *et al.*, "Infrared light management in high-efficiency silicon heterojunction and rear-passivated solar cells," *J. Appl. Phys.*, vol. 113, 2013, Art. ID. 013107.
- [17] Z. C. Holman *et al.*, "Parasitic absorption in the rear reflector of a silicon solar cell: Simulation and measurement of the sub-bandgap reflectance for common dielectric/metal reflectors," *Sol. Energy Mater. Sol. Cells*, vol. 120, pp. 426–430, 2014.
- [18] Z. C. Holman, S. De Wolf, and C. Ballif, "Improving metal reflectors by suppressing surface plasmon polaritons: A priori calculation of the internal reflectance of a solar cell," *Light: Sci. Appl.*, vol. 2, 2013, Art. ID. e106.
- [19] A. Dabirian *et al.*, "Tuning the optoelectronic properties of ZnO:Al by addition of silica for light trapping in high-efficiency crystalline Si solar cells," *Adv. Mater. Interfaces*, vol. 3, 2016, Art. ID. 1500462.
- [20] K. O. Davis *et al.*, "Investigation of the internal back reflectance of rear-side dielectric stacks for c-Si solar cells," *IEEE J. Photovolt.*, vol. 3, no. 2, pp. 641–648, Apr. 2013.
- [21] M. S. Branham *et al.*, "15.7% efficient 10- μm -thick crystalline silicon solar cells using periodic nanostructures," *Adv. Mater.*, vol. 27, pp. 2181–2188, 2015.
- [22] D. Kray, M. Hermle, and S. W. Glunz, "Theory and experiments on the back side reflectance of silicon wafer solar cells," *Prog. Photovolt.: Res. Appl.*, vol. 16, pp. 1–15, 2008.
- [23] S. C. Baker-Finch and J. R. McIntosh, "One-dimensional photogeneration profiles in silicon solar cells with pyramidal texture," *Prog. Photovolt.: Res. Appl.*, vol. 20, pp. 51–61, 2012.
- [24] M. Peters, M. Rüdiger, H. Hauser, M. Hermle, and B. Bläsi, "Diffraction gratings for crystalline silicon solar cells—Optimum parameters and loss mechanisms," *Prog. Photovolt.: Res. Appl.*, vol. 20, pp. 862–873, 2012.
- [25] Y. Zhang, B. Jia, Z. Ouyang, and M. Gu, "Influence of rear located silver nanoparticle induced light losses on the light trapping of silicon wafer-based solar cells," *J. Appl. Phys.*, vol. 116, 2014, Art. ID. 124303.
- [26] A. Ingenito, O. Isabella, and M. Zeman, "Experimental demonstration of 4n2 classical absorption limit in nanotextured ultrathin solar cells with dielectric omnidirectional back reflector," *ACS Photon.*, vol. 1, pp. 270–278, 2014.
- [27] Y. Tao *et al.*, "Large area tunnel oxide passivated rear contact n-type Si solar cells with 21.2% efficiency," *Prog. Photovolt.: Res. Appl.*, vol. 24, pp. 830–835, 2016.
- [28] Y. Tao *et al.*, "Fully ion-implanted and screen-printed 20.2% efficient front junction silicon cells on 239 cm² n-type CZ substrate," *IEEE J. Photovolt.*, vol. 4, no. 1, pp. 58–63, Jan. 2014.
- [29] G. Yang, A. Ingenito, N. van Hameren, O. Isabella, and M. Zeman, "Design and application of ion-implanted polySi passivating contacts for interdigitated back contact c-Si solar cells," *Appl. Phys. Lett.*, vol. 108, 2016, Art. ID. 033903.
- [30] D. L. Young *et al.*, "Interdigitated back passivated contact (IBPC) solar cells formed by ion implantation," *IEEE J. Photovolt.*, vol. 6, no. 1, pp. 41–47, Jan. 2016.
- [31] B. Nemeth *et al.*, "Polycrystalline silicon passivated tunneling contacts for high efficiency silicon solar cells," *J. Mater. Res.*, vol. 31, pp. 671–681, 2016.
- [32] J. Bullock *et al.*, "Amorphous silicon passivated contacts for diffused junction silicon solar cells," *J. Appl. Phys.*, vol. 115, 2014, Art. ID. 101063.
- [33] D. Yan, A. Cuevas, Y. Wan, and J. Bullock, "Passivating contacts for silicon solar cells based on boron-diffused recrystallized amorphous silicon and thin dielectric interlayers," *Sol. Energy Mater. Sol. Cells*, vol. 152, pp. 73–79, 2016.

- [34] M. Topič, M. Sever, B. Lipovšek, A. Čampa, and J. Krč, "Approaches and challenges in optical modelling and simulation of thin-film solar cells," *Sol. Energy Mater. Sol. Cells*, vol. 135, pp. 57–66, 2015.
- [35] M. Sever, J. Krc, A. Campa, and M. Topic, "Rigorous modelling of light scattering in solar cells based on finite element method and Huygens' expansion," *Opt. Express*, vol. 23, pp. A1549–A1563, Nov. 2015.
- [36] R. Santbergen and R. J. C. van Zolingen, "The absorption factor of crystalline silicon PV cells: A numerical and experimental study," *Sol. Energy Mater. Sol. Cells*, vol. 92, pp. 432–444, 2008.
- [37] S. Altazin *et al.*, "Design of perovskite/crystalline-silicon tandem solar cells," in *Proc. 32nd Eur. Photovolt. Sol. Energy Conf.*, 2016, pp. 1276–1279.
- [38] A. Dabirian and N. Taghavinia, "Theoretical study of light trapping in nanostructured thin film solar cells using wavelength-scale silver particles," *ACS Appl. Mater. Interfaces*, vol. 7, pp. 14926–14932, Jul. 2015.
- [39] E. Yablonovitch, "Statistical ray optics," *J. Opt. Soc. Amer.*, vol. 72, pp. 899–907, 1982.
- [40] M. A. Green, "The passivated emitter and rear cell (PERC): From conception to mass production," *Sol. Energy Mater. Sol. Cells*, vol. 143, pp. 190–197, 2015.
- [41] J. M. Weber, *Handbook of Optical Materials*. Boca Raton, FL, USA: CRC Press, 2003.
- [42] Y. Liu, G. Bartal, and X. Zhang, "All-angle negative refraction and imaging in a bulk medium made of metallic nanowires in the visible region," *Opt. Express*, vol. 16, pp. 15439–15448, 2008.
- [43] W. C. Chew, *Waves and Fields in Inhomogeneous Media*. Piscataway, NJ, USA: IEEE Press, 1995.
- [44] M. Boccard, C. Battaglia, F. J. Haug, M. Despeisse, and C. Ballif, "Light trapping in solar cells: Analytical modeling," *Appl. Phys. Lett.*, vol. 101, 2012, Art. ID. 151105.
- [45] B. Demareux *et al.*, "Atomic-layer-deposited transparent electrodes for silicon heterojunction solar cells," *IEEE J. Photovolt.*, vol. 4, no. 6, pp. 1387–1396, Nov. 2014.
- [46] V. R. Almeida, Q. Xu, C. A. Barrios, and M. Lipson, "Guiding and confining light in void nanostructure," *Opt. Lett.*, vol. 29, pp. 1209–1211, 2004.
- [47] A. Celzard *et al.*, "Critical concentration in percolating systems containing a high-aspect-ratio filler," *Phys. Rev. B*, vol. 53, pp. 6209–6214, 1996.
- [48] I. Balberg, C. H. Anderson, S. Alexander, and N. Wagner, "Excluded volume and its relation to the onset of percolation," *Phys. Rev. B*, vol. 30, pp. 3933–3943, 1984.
- [49] C. A. Foss, G. L. Hornyak, J. A. Stockert, and C. R. Martin, "Template-synthesized nanoscopic gold particles: Optical spectra and the effects of particle size and shape," *J. Phys. Chem.*, vol. 98, pp. 2963–2971, 1994.
- [50] J. Chen *et al.*, "Porous anodic alumina with low refractive index for broadband graded-index antireflection coatings," *Appl. Opt.*, vol. 51, pp. 6839–6843, 2012.
- [51] L. Fanni *et al.*, "Tuning the porosity of zinc oxide electrodes: From dense to nanopillar films," *Mater. Res. Express*, vol. 2, 2015, Art. ID. 075006.

Authors' photographs and biographies not available at the time of publication.